Wideband Circularly Polarized Antenna with In-Lens Polarizer for High-Speed Communications

Arias Campo, Marta; Carluccio, Giorgio; Blanco, Darwin; Litschke, Oliver; Bruni, Simona; Llombart, Nuria

DOI
10.1109/TAP.2020.3008638

Publication date
2021

Document Version
Accepted author manuscript

Published in
IEEE Transactions on Antennas and Propagation

Wideband Circularly Polarized Antenna with In-Lens Polarizer for High-Speed Communications

Marta Arias Campo, *Student Member, IEEE,* Giorgio Carluccio, *Member, IEEE,* Darwin Blanco, Oliver Litschke, Simona Bruni, and Nuria Llombart, *Fellow, IEEE*

***Abstract*— In this contribution, a broadband G-band leaky-wave fed lens antenna with an integrated dielectric grid polarizer is presented. The proposed wideband polarizer unit cell geometry enables its fabrication at frequencies higher than 100GHz, presenting high transmission properties and low axial ratio (AR). A quasi-analytical technique based on Spectral Green's Functions combined with a numerical Floquet mode solver is used to optimize the lens aperture efficiency and axial ratio. The proposed technique is validated via full wave simulations. A design is proposed in low dielectric permittivity material, achieving full-wave simulated aperture efficiency higher than 75% over 44% relative bandwidth, and an AR lower than 3dB over 35% relative bandwidth. The antenna is able to achieve multiple directive circularly-polarized beams, when fed by a focal plane array, preserving the AR bandwidth. A prototype has been fabricated and measured, exhibiting an excellent match with quasi-analytic and full-wave simulations.**

***Index Terms*—Polarizer, circular polarization, dielectric gratings, leaky-wave, lens antenna, wideband communications.**

I. Introduction

THE booming demand for high-speed wireless communications calls for a revolution in the way the networks and systems are conceived. The saturation in the use of lower frequency bands and the limited radiofrequency (RF) bandwidth that they provide have led to the 5G technology emergence. This new generation relays on the use of higher frequency bands (K-, Ka-, Q-bands), with larger RF bandwidth availability and therefore higher link capacities. The way towards the use of higher frequencies (D-, G- or H-bands) will continue in the next years, requiring the development of system architectures, active and passive devices to enable the efficient use of the mm-wave spectrum. The higher path-loss in these frequency bands needs to be compensated with the use of high-gain antennas. On top of that, due to the limited output power in the mm-wave and terahertz transmitters, it is crucial to maximize the efficiency in the last system stages, and especially in the antennas.

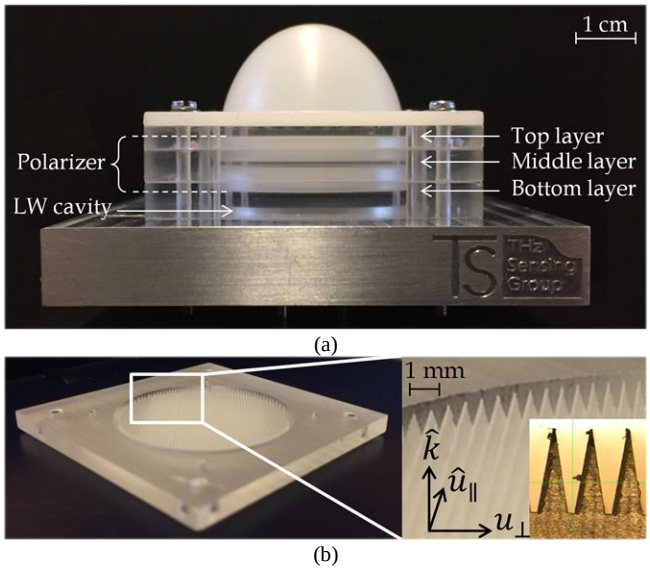

Fig. 1. a) CP antenna prototype. From bottom to top: split-block waveguide, integrated polarizer in Topas material and lens fabricated with HDPE. b) Bottom polarizer layer and side view of the polarizer pyramidal gratings.

In [1] an efficient, wide-band linear-polarized (LP) lens antenna with a leaky-wave feeder was proposed in G-band (140–220GHz) to be used in a Fly's Eye architecture, suitable for point-to-multipoint and dense small cells scenarios [2]. In order to enhance the wireless link efficiency, especially in scenarios with moving terminals, circularly polarized lens antennas are even better candidates to be used as single elements in the Fly's Eye lens arrays, as they minimize the loss due to polarization misalignment. However, wideband, low loss and cost-effective concepts are needed to generate circular polarization (CP), in order not to compromise the performance reached with the LP lenses. The challenge to achieve these goals in the mm-wave and sub-mm-wave bands is addressed in this contribution.

Manuscript received XXX; revised XXX; accepted XXX. Date of publication XXX; date of current version XXX. This work was supported in part by the European Union through the ERC Starting Grant LAA-THz-CC under Grant 639749 and in part by the company IMST GmbH in Germany.

Marta Arias Campo is with the THz Sensing Group, Delft University of Technology, 2628 CD Delft, The Netherlands and also with IMST GmbH, 47475 Kamp-Lintfort, Germany (e-mail: m.ariascampo@tudelft.nl; arias@imst.de).

Giorgio Carluccio is with NXP Semiconductors, 5656 AE, Eindhoven, The Netherlands.

Darwin Blanco is with Ericsson AB, 417 56 Gothenburg, Sweden.

Oliver Litschke and Simona Bruni are with IMST GmbH, 47475 Kamp-Lintfort, Germany.

Nuria Llombart is with the THz Sensing Group, Delft University of Technology, 2628 CD Delft, The Netherlands.

Many linear to circular polarization conversion concepts can be found in the literature up to 60GHz ([3]–[13]). However, this is not the case for mm-wave frequencies higher than 100GHz, where only few examples have been published to our knowledge ([16]–[24]). Waveguide polarizers are widely used as horn feeders, achieving large 3dB AR relative bandwidths (>20%) by means of grooves [3], dielectric [4], [5] or metallic septa [6]. However, the tolerances in the fabrication of such structures as well as in the mounting of the septum inside the waveguide are critical in frequencies higher than 100GHz. CP horn antennas have been as well proposed, based on Antipodal Tapered Slot Antennas (ATSA) [7], [16] or hexagonal waveguides [17], reaching excellent 3dB AR relative bandwidths (>35%) but gains lower than 18dB. Higher gain could be reached when using them as reflector feeds, resulting however in a more bulky solution, not suitable for a planar configuration [1]. Horn arrays have as well been proposed in [8] at 30GHz or [18] at 140GHz, reaching gains higher than 30 dB but compromising the 3dB AR bandwidth (<16%).

Several approaches in the literature make use of LP feeders illuminating linear-to-circular add-on polarization converters. Many of those are based on single- or multi-layer designs with metallic sub-wavelength structures, which present different susceptances for orthogonal linear polarizations [9]–[11], [19]. When the LP field from the source impinges the polarizer with a polarization rotated 45deg with respect to the polarizer axis, the two incident orthogonal in-phase field components propagate along the polarizer experimenting ideally negligible modifications in the amplitude, but different phase shifts, reaching 90deg and so originating circular polarization in the transmitted wave. Although they achieve large 3dB AR relative bandwidths (>25%), the use of very thin metal printed structures makes their fabrication impossible in standard PCB technology for frequency bands higher than 100GHz. The design presented in [19] at 325GHz is fabricated with complex wafer based silicon micromachining techniques, not suitable for low-cost mass-production. The mentioned fabrication issues are as well present in circularly polarized transmitarrays [12] and reflectarrays [13].

Polarization converters based on dielectric gratings present higher potential to become a cost-effective and, at the same time, high-performing solution at mm- and sub-mm wave frequencies. We have therefore taken this concept as starting point in our work. Their working principle is based on the effective dielectric permittivity anisotropy originated by the asymmetric dielectric gratings, which results in different propagations constants for orthogonal LP field components. The examples proposed in the literature are mostly based on rectangular gratings, either in low relative permittivity for mm-wave applications [14], [15] or in high relative permittivity in optics [20], [21]. Whereas high relative permittivity gratings present lower profile and smaller bandwidth, the opposite properties appear for low relative permittivity polarizers, leading to high aspect ratios which encumber their manufacturing at frequencies higher than 100 GHz. Metal grating polarizers, based on the reflection of orthogonal polarizations with 90deg of phase shift, are as well used in terahertz bands [22]. However, they present a narrow bandwidth and cannot be integrated into a lens antenna, resulting in a more bulky solution. In [23] a 130GHz tunable liquid crystal polarizer concept working in reflection was presented, with high insertion loss due to the lossy material (>4dB), and with narrowband AR (<3%).

Regarding CP antenna designs with multi-beam capability, not many examples are present in the literature. The mentioned transmitarrays and reflectarrays, apart from the named fabrication issues, present very low aperture efficiencies, hindering a compact solution. In [24], a concept based on CP patches feeding an integrated elliptical Rexolite lens, exhibits a very small 3dB AR bandwidth (2.6%). In [5], a homogeneous spherical Teflon lens fed with CP horns is presented, with good AR properties but low aperture efficiency (<37%). In [15], the rectangular dielectric gratings are integrated in an extended hemispherical lens, achieving 29% 3dB AR bandwidth and 21 dB of gain at 60 GHz. The side-lobe level is however high (-12dB) due to the poor illumination of the lens. Besides, despite the low directivity achieved, high dielectric losses are present (>3dB) due to the material used in the 3D printing fabrication.

In this contribution, an add-on polarizer based on the dielectric-grating concept is proposed to be integrated inside an elliptical plastic lens (Fig. 1a) and fed by the resonant LWA presented in [1]. A new polarizer unit cell geometry is proposed, enabling the fabrication of wideband low dielectric permittivity polarizer gratings at G-band, with low-cost, low-loss plastic materials and standard milling techniques. In addition, this geometry improves the bandwidth and transmission with respect to the standard rectangular-grating used in [15]. Thanks to the LWA feeder, which radiates most of the energy below the dielectric-air critical angle, total reflections in the lens dielectric-polarizer interface are avoided. The elliptical lens provides the antenna with high gain (>30 dB) and steering capability, making it suitable for high-speed communication systems.

The combination of a high-directivity lens (diameter bigger than $15\lambda_0$) and a polarizer (containing sub-wave length structures) in a single full-wave (FW) simulation, results in an extremely time-consuming model. In this contribution, in order to provide a fast optimization of the feed-polarizer-lens system, a quasi-analytical model based on Spectral Green´s Functions (SGFs) and an analysis of the lens in reception [1], combined with a single unit-cell Floquet mode solver has been developed and used. The quasi-analytic approach for the lens analysis allows extracting the CP aperture efficiency and axial ratio after the lens. The fabricated antenna, optimized with this quasi-analytical method, achieves full-wave simulated aperture efficiency higher than 75% over a 44% relative bandwidth and an axial ratio lower than 3 dB over a 35% relative bandwidth, with dielectric losses lower than 0.65dB.

The paper is organized as follows: Section II describes the overall antenna concept, the new polarizer grating geometry, and the analysis and optimization methodology applied; Section III shows the antenna prototype design and simulation

results; Section IV describes the measurement procedure used to characterize the antenna CP radiation patterns, AR, and gain.

II. Circularly Polarized Lens Antenna Concept

In this section, the concept of the dielectric lens with embedded polarizer, CP lens, is explained. Circular polarization is achieved inside the dielectric lens by placing a dielectric-grating polarizer on top of a resonant Leaky-Wave feeder, as shown in Fig. 1a. A novel wideband polarizer unit cell geometry, suitable to be fabricated at sub-mm wavelengths, is introduced here. In transmission, the lens is illuminated by a CP primary field, collimating it to achieve high-gain.

The fast quasi-analytical methodology applied to optimize the full feed-polarizer-lens system performance is as well presented in this section. The CP primary patterns are calculated inside the lens by evaluating the multi-layer anisotropic structure with SGF. The optimization of the CP lens aperture efficiency and AR calculation are performed by means of an analysis of the antenna in reception.

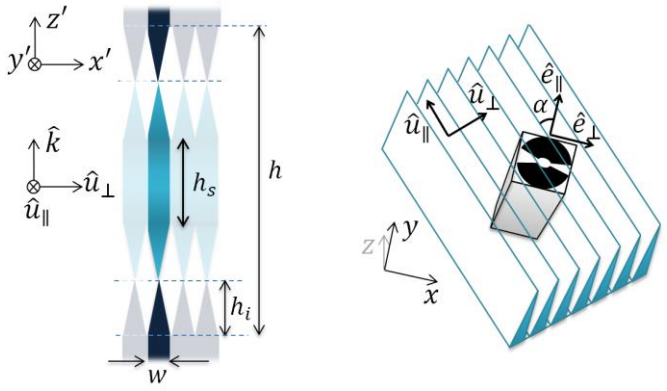

(a) (b)

Fig. 2. a) Polarizer unit cell. The blue color represents the dielectric, whereas the white color the air. The dashed lines mark the separation of the polarizer in three pieces for its fabrication. $h = 4.26\lambda_0$, $h_i = 0.76\lambda_0$, $h_s = 1.2\lambda_0$ and $w = 0.5\lambda_d$, being λ_0 the free-space wavelength at f_0=180GHz and $\lambda_d = \lambda_0/\sqrt{\varepsilon_r}$. b) Wave-guide cross-section and double-slot with polarizer grid on top, oriented with an angle $\alpha = 45$deg with respect to the double slot linear polarization $\hat{e}_\parallel$.

A. In-Lens Polarizer: Unit Cell

An add-on polarizer using dielectric gratings has been chosen to be embedded in the lens, due to its large bandwidth properties and its suitability for a cost-effective manufacturing at such small wave-lengths. The dielectric gratings are fabricated in the same low relative dielectric permittivity ε_r material as the lens ($\varepsilon_r = 2.3$). The choice of this low ε_r improves the bandwidth of the polarizer transmission coefficients, enhancing as well the AR bandwidth. However, in terms of birefringence, lower ε_r values provide a lower contrast between the effective permittivity for the perpendicular and parallel field components ($\hat{u}_\parallel$ and $\hat{u}_\perp$ in Fig. 1b and Fig. 2b). This leads to higher grating heights, h in Fig. 2a, required to achieve the aimed 90deg phase shift between the orthogonal LP components. On the other hand, the unit cell width or period, w, should be small enough to avoid grating lobes (~$\lambda_d/2$). When choosing a standard rectangular grating geometry, these conditions result in a unit cell aspect ratio, h/w, higher than 14. The fabrication of such high h/w represents a big challenge at frequencies above 100GHz. In order to facilitate the fabrication of the polarizer with standard milling techniques, a polarizer geometry with N separate layers, each with a thickness of $h_i = h/N$, is proposed. These layers are composed by identical extruded pyramids, piled to form the complete polarizer unit cell, as show in Fig. 2a. The pyramids' slope, determined by the milling tool tip angle, sets the maximum achievable height, and therefore phase shift, per layer. For our current implementation, the polarizer is made out of N=4 layers to reach the 90deg phase shift. Further details regarding the polarizer fabrication have been given in [25]. The resulting polarizer unit cell geometry is shown in Fig. 2a. It can be fabricated in three parts: the bottom and top part, with gratings on one side, and the central part with gratings on both sides, as can be recognized as well in Fig. 1a. This tapered form provides the gratings with mechanical stability and represents as well a smooth transition between the air and plastic material characteristic impedances. This enhances the polarizer transmission properties w.r.t. a rectangular corrugation, making it unnecessary to perform a fine lateral alignment between the different polarizer layers.

The polarizer transmission properties have been analyzed by means of Floquet simulations for a single unit cell, with periodic boundary conditions. A 4-port S-parameters matrix can be extracted for each plane-wave angle of incidence, describing the coupling between TE and TM modes.

B. LWA Feeder with Add-on Polarizer

The CP feeder, shown in Fig. 3a, consists of a linearly-polarized (LP) LWA feeder with the proposed add-on polarizer on top, as displayed in Fig. 2b. The LWA contains a resonant air cavity, which can be seen in Fig. 1a, between a ground plane and a denser dielectric ($\varepsilon_r = 2.3$). As explained in [1], along this air gap three leaky-wave modes, TM_0, TM_1, and TE_1, propagate radially, radiating energy into the lens dielectric. This effect increases the antenna effective area, and therefore its directivity. The LW modes radiate with a propagation constant $\beta = k_0\sqrt{\varepsilon_r}\sin\theta_{LW} < k_0$, being θ_{LW} the LW mode radiation angle [26]. This results in $\theta_{LW} < \sin^{-1} 1/\sqrt{\varepsilon_r} = \theta_c^f$, where θ_c^f is the air-dielectric critical angle (Fig. 3a). For $\varepsilon_r = 2.3$, θ_c^f appears at 41deg, and as a consequence the patterns radiated by this feed inside the lens (primary patterns), present a taper higher than -12dB at this angle. The polarizer presents effective $\varepsilon_r > 1$ for both orthogonal field components, and therefore the critical angle in the interface between the polarizer and the dielectric medium, θ_c^p in Fig. 3a, is always higher than θ_c^f. Thanks to the LWA properties, the polarizer is only illuminated with incident angles lower than θ_c^f ($\theta_{LW} < \theta_c^f$). This avoids significant total reflections in the interface between the lens material and the polarizer gratings. The cavity is excited by a standard wave-guide tapered to a squared wave-guide, on top

of which a double-slot is placed. The double-slot shapes the pattern to optimize the illumination efficiency, and achieves the impedance matching to the waveguide [1].

The add-on polarizer based on dielectric gratings is placed on top of the LP LWA at a coordinate $z = z_{bot}$ (Fig. 3a), which is high enough to preserve the LW propagation properties. The polarizer gratings are oriented with an angle of 45deg w.r.t. the LP LWA polarization (Fig. 2b).

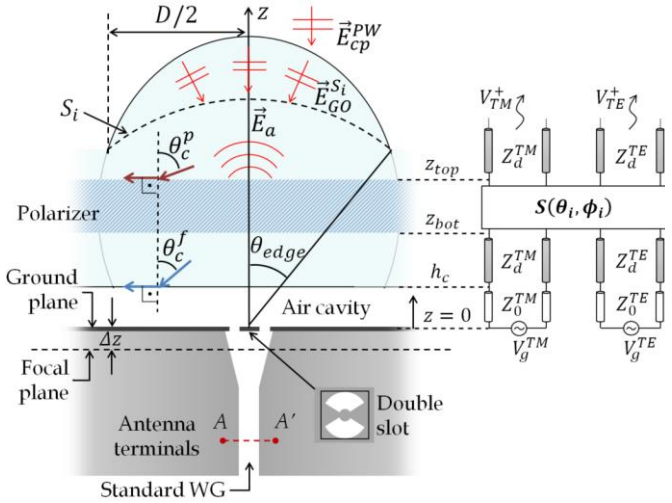

Fig. 3. Left: Main parameters of the elliptical lens geometry with integrated polarizer, and LW feeder. Optimized values: $h_c = 0.56\lambda_0$, $z_{bot} = 2.27\lambda_0$, $z_{top} = 6.53\lambda_0$ $\theta_{edge} = 40$deg, $\Delta z = -2.8$mm. The fields used for the lens aperture efficiency and axial ratio calculation are as well represented here ($\vec{E}_a, \vec{E}_{GO}^{S_i}$ and $\vec{E}_{cp}^{PW}$). Right: Equivalent transmission line model applied for the CP primary pattern calculation.

The resulting anisotropic multilayer structure shown in Fig. 3a has been analyzed with the SGF approach discussed in the Appendix, including the polarizer unit cell S-parameters estimated with FW Floquet-mode simulations. In this way, the CP radiation patterns of the LWA feeder after propagating through the polarizer (CP primary patterns) can be calculated inside the semi-infinite dielectric medium on top of the polarizer (Fig. 3).

C. Optimization of Lens with Integrated Polarizer

In order to obtain the high gain required for a wide-band communications scenario, a truncated elliptical lens [1] is placed on top of the CP feeder (LWA feeder + polarizer). Once the CP primary patterns have been calculated, the elliptical lens and feeder parameters can be optimized by applying an analysis of the antenna in reception, based on the same methodology described in [27] and applied in [1]. This enables a fast optimization for the feed-polarizer-lens system, avoiding time-consuming FW simulations. The LW cavity height, h_c, the double slot geometry, the feed z position with respect to the focal plane, Δz, and lens truncation angle, θ_{edge} (Fig. 3), are the variables to maximize the CP lens aperture efficiency, η_{ap}. The lens θ_{edge} determines its focal length F for a given lens diameter D, as the lens eccentricity is given by its ε_r as $e = 1/\sqrt{\varepsilon_r}$ [1].

The geometry and fields used in this evaluation are shown in Fig. 3. In this analysis, the voltage generated by an ideal CP plane wave at the open circuited antenna terminals AA', V_{oc}, in the antenna evaluated in reception, is derived to calculate the antenna efficiency η_{ap}. V_{oc} is determined by performing a reaction integral over the surface S_i, inside the lens, between the CP primary patterns evaluated in transmission, $\vec{E}_a$, and the incoming field $\vec{E}_{GO}^{S_i}$ from the CP plane wave as

$$V_{oc} I_{tx} = \frac{2}{\zeta_d} \int_0^{2\pi} \int_0^{\theta_{edge}} \vec{E}_{GO}^{S_i}(\theta,\phi) \cdot \vec{E}_a^{GP}(\theta,\phi) e^{jk_d \Delta z \cos\theta} \, dS \quad (1)$$

where I_{tx} is the amplitude of the electric current feeding the antenna in transmission, θ_{edge} is the lens rim angle from the focus, $\zeta_d = \frac{\zeta_0}{\sqrt{\varepsilon_r}}$ and ζ_0 the wave impedance in vacuum. $\vec{E}_a^{GP}$ is calculated with the phase reference in the LW ground plane, and the term $e^{jk_d \Delta z \cos\theta}$ represents the z-displacement of the ground plane w.r.t. the lens focal plane, applied to place the actual feeder phase centre on the lens focus ($\vec{E}_a = \vec{E}_a^{GP} e^{jk_d \Delta z \cos\theta}$). As explained in [1], I_{tx} can be arbitrary chosen (e.g. $I_{tx} = 1A$, becoming $V_{oc} I_{tx} = V_{oc}$). The steps to derive the equation (1) are explained with detail in [1]. As we are aiming for a CP field, the ideal incident plane-wave, $\vec{E}_{cp}^{PW}$ (Fig. 3), is in this case circularly polarized. In this way, two orthogonally CP plane waves are defined as

$$\vec{E}_{RH}^{PW} = \frac{1}{\sqrt{2}}(\hat{x} + j\hat{y}) \quad (2a)$$

$$\vec{E}_{LH}^{PW} = \frac{1}{\sqrt{2}}(\hat{x} - j\hat{y}) \quad (2b)$$

being $\vec{E}_{RH}^{PW}$ right-handed circularly polarized and $\vec{E}_{LH}^{PW}$ left-handed circularly polarized, with propagation vector $-\hat{z}$. The corresponding $\vec{E}_{GO}^{S_i}$ can be evaluated analytically as derived in [28].

η_{ap} is estimated relating the power captured by the lens from the co-polarized CP plane-wave impinging the lens from broadside, P_{in}, to the power which is actually delivered to the load at the feed, P_L as

$$\eta_{ap} = \frac{P_L}{P_{in}} = \frac{|V_{oc}|^2}{16 P_{rad} P_{in}} \quad (3)$$

where $P_{in} = 1/(2\zeta_0)|E_0^{PW}|^2 A_{lens}$, being $A_{lens} = \pi D^2/4$ the projected area for a lens with diameter D (Fig. 3), and P_{rad} is the power radiated by the antenna in transmission. The resulting η_{ap} includes the taper, phase, reflection and spill-over efficiencies, being equivalent to the difference between the achieved directivity and the maximum directivity for this circular aperture.

In order to derive the lens axial ratio, V_{oc} is calculated for both orthogonal CP plane waves. The far-field at broadside for each CP component is proportional to its corresponding V_{oc} (reciprocity theorem), and therefore the lens axial ratio at broadside can be approximated e.g. for a right-handed circularly polarized antenna similarly as defined in [29]

$$\mathrm{AR} = \frac{|V_{oc}^{RH}| + |V_{oc}^{LH}|}{|V_{oc}^{RH}| - |V_{oc}^{LH}|} \quad (4)$$

III. Prototype Design And Fabrication

Applying the described analysis methodology based on SGF and an analysis of the antenna in reception, a CP lens antenna has been designed in G-band, centered in 180GHz, with a diameter $D = 18\lambda_0$ (Fig. 3). In this section, the final geometry and simulation results are shown for the polarizer unit cell, the CP feeder radiating in a semi-infinite dielectric medium and, finally, for the complete CP lens antenna.

A. Unit Cell Performance

The unit cell dimensions for the polarizer are reported in Fig. 2a. The unit cell period w avoids the grating lobes for incident angles up to 52deg, until 200GHz. The resulting pyramid h_i/w is 2.3. The polarizer S-parameters are estimated from Floquet-mode simulations performed with CST Studio Suite [30] for the unit cell, using the first two Floquet modes (TE_1 and TM_1). As shown in Fig. 4a, the polarizer unit cell is almost "transparent" to the incident wave amplitude up to $\theta_c^f = 41$deg, after which the LWA is radiating very low power. The AR is lower than 3dB in both principal planes for incident angles lower than 25deg. Fig. 4b shows the unit cell AR over the whole frequency band, for different incident angles. In this figure, the AR is displayed for unit cells with aligned and fully misaligned pyramid layers, showing the robustness of the concept against misalignment.

B. LWA Feeder with Polarizer: Radiation Patterns and AR

Fig. 5 shows the far-field patterns of the LWA with the polarizer radiating in a semi-infinite dielectric medium (Fig. 3a), calculated applying the SGF model discussed in the Appendix. The validation with FW simulations with EMPIRE XPU [31] shows an excellent agreement with the SGF results, in both phase and amplitude, over the whole frequency band. The radiation patterns for the CP LW feeder are very close to the LP ones [1], thanks to the polarizer good transmission properties and low axial ratio. This can be seen as well in the directivity comparison for the feeder with (CP) and without polarizer (LP), which differ in maximum 1dB, as shown in Fig. 6. The simulated feeder maximum directivity over frequency has a variation lower than 2dB in the whole band, being the AR at broadside lower than 3dB from 150GHz to 220GHz (Fig. 6).

C. Lens with Integrated Polarizer: Radiation Patterns and AR

Using the analysis in reception described in Section II.C, the CP lens geometry has been optimized to maximize η_{ap}. As the polarizer does not significantly modify the primary patterns with respect to the LP ones (Fig. 5), the double-slot geometry and lens truncation angle θ_{edge} have not been modified w.r.t. the LP design in [1]. However, the CP feeder phase center changes with respect to the LP feeder, due to the polarizer lower effective ε_r, being the optimum feeder phase center position with respect to the lens focal plane $\Delta z = -2.8$mm. The final results for the lens η_{ap} and AR have been validated by means of FW simulations performed with EMPIRE XPU (with multiple reflections), showing very good agreement. Fig. 7a shows that the lens η_{ap}, is not degraded with the use of the polarizer, remaining very close to the η_{ap} for the linearly polarized lens. In Fig. 7b, the resulting AR is reported, compared as well with the AR evaluated with the lens FW simulated radiation patterns. Results show a lens $\eta_{ap} > 75\%$ over 44% bandwidth and AR < 3 dB over 35% bandwidth.

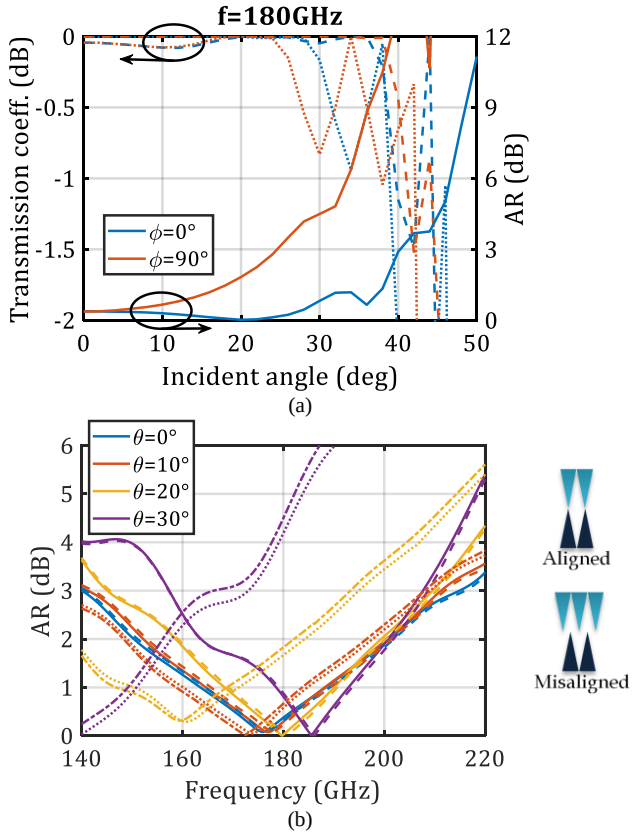

Fig. 4. a) Left axis: unit cell transmission coefficients of the fundamental Floquet-mode vs. plane-wave incident angles at 180GHz. Dashed line: TM mode; dotted line: TE mode. Right axis: AR calculated from the complex unit cell transmission coefficients. b) Unit cell AR over frequency for different angles of incidence, evaluated from the Floquet-mode simulations. Solid line: $\phi = 0$deg incidence with aligned pyramids; dashed line: $\phi = 0$deg misaligned pyramids; dotted-dashed line: $\phi = 90$deg aligned pyramids; dotted line: $\phi = 90$deg misaligned pyramids. The unit cell coordinate system is taken as in Fig. 2b, aligned with its periodicity.

Fig. 8 shows the CP FW simulated radiation patterns at broadside for the lens with integrated polarizer, with side-lobe levels (SLL) lower than -15 dB up to 200 GHz. The feeder has been displaced off-focus, as explained in [1], in order to perform beam steering with the elliptical lens. By placing the polarizer below the lens, the polarizer is illuminated in the same manner regardless which is the feed position over the lens focal plane. In this way, the feeder AR, and therefore also the lens AR bandwidth, do not change when performing beam steering, as it can be appreciated in Fig. 7c. Moreover, the impact of multiple reflections in the AR is in case of the steered beams lower, as the reflected waves do not propagate in the main beam direction. Fig. 9 shows the radiation patterns for the steered beams, with very similar SLL to the LP patterns presented in [1]. Fig. 10 displays the maximum gain over frequency for the broadside and steered beams, showing

as well very similar performance to the LP lens. This fact implies that the maximum steering angle achieved with the lens, or number of beams suitable to cover a communication scenario, as discussed in [1], is not degraded w.r.t. the LP lens.

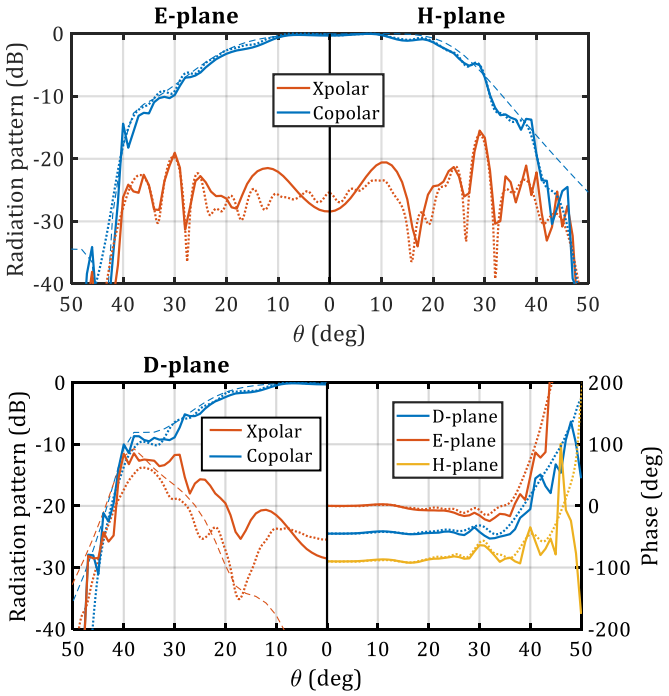

Fig. 5. Far-field amplitude and phase for LWA feed with polarizer radiating in infinite medium. Solid line: SGF model. Dotted line: FW simulations. Dashed line (in radiation pattern plots): linear polarized feed (without polarizer), SGF model. E-, H- and D-planes are defined here with respect to the LP feeder polarization.

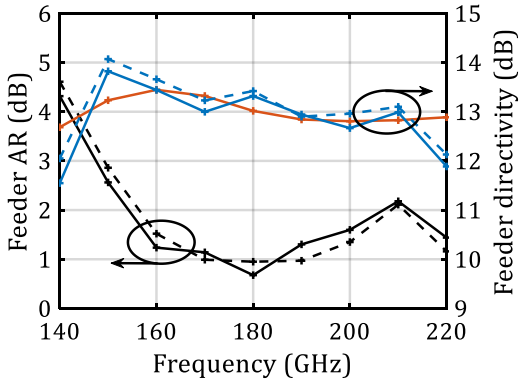

Fig. 6. Left axis: Axial ratio at broadside for LWA feeder with polarizer. Right axis: LWA feeder directivity with and without polarizer (linearly polarized). Solid line: SGF model. Dashed line: FW simulations. Red line: linearly polarized feeder directivity (without polarizer).

In Fig. 11 the CP lens antenna reflection coefficient seen from the standard waveguide flange is displayed, being this -10dB over the whole frequency band.

The CP lens antenna prototype makes use of the same split-block waveguide and double slot manufactured for the LP design in [1]. The polarizer has been fabricated in Topas material, on top of which a HDPE lens has been placed (Fig. 1a), both materials presenting $\varepsilon_r = 2.3$. HDPE has been chosen for the lens fabrication due to its very low loss properties ($\tan\delta = 3.4 \times 10^{-4}$); Topas material ($\tan\delta = 1.2 \times 10^{-3}$) has been chosen for the polarizer fabrication, as its hardness facilitates the milling process [25]. The maximum dielectric loss in the lens, evaluated with the FW simulated gain, is 0.65dB at 220GHz.

IV. Measurements

In this section, the measurement campaign carried out to characterize the CP lens antenna prototype is described.

The antenna reflection coefficient has been measured at the split-block standard waveguide interface, being the results in agreement with simulations (Fig. 11). In order to make a first validation of the antenna polarization performance, the lens self-coupling (power reflected from a metal plate) has been measured, using an approach similar to [32], but placing the metal plate directly in the near-field instead of the far-field. In order to validate the lens radiation efficiency η_{rad} (to calculate the antenna gain) and with the aim of performing a first AR measurement, a phase-amplitude method has been applied [33], measuring the coupling to the LP lens in [1]. In this approach, the LP lens is rotated 90deg to measure both orthogonally LP field components. Here, a very accurate relative phase characterization and positioning between the two LP measurements is needed to characterize the CP fields. The strategy to perform the phase calibration between the two measurements, which is very challenging in this frequency band, is explained in this section. Profiting from this calibration and using as well the phase-amplitude method, two near-field measurements with a LP near-field probe were performed for each beam to obtain the CP radiated fields. The lens radiation patterns, maximum gain, and AR validation by means of coupling and near-field measurements is presented for the broadside and steered beams, with an excellent agreement with quasi-analytic and FW simulation results.

A. Antenna Self-Coupling (Measurement in Reflection)

A first verification of the antenna polarization purity has been performed by measuring the signal reflected on a metal plate, coming back to the CP lens (setup in Fig. 12a). This measurement is equivalent to the one of the transmission between two orthogonally CP polarized lenses.

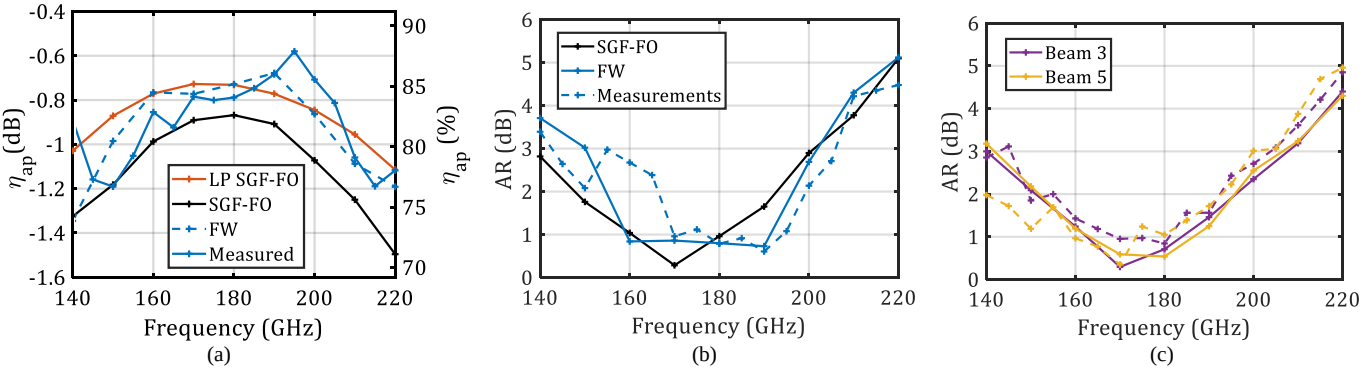

Fig. 7. a) Broadside aperture efficiency for the CP lens. In red, the SGF-FO simulations for the LP lens are reported for reference. b) CP lens axial ratio at broadside. c) CP lens AR for the beams steering at 8.4deg (beam 3) and 16deg (beam5) (corresponding respectively to feed displacements, d = 0.09D and 0.19D). Solid line: FW simulations; dashed line: far-field from near-field measurements.

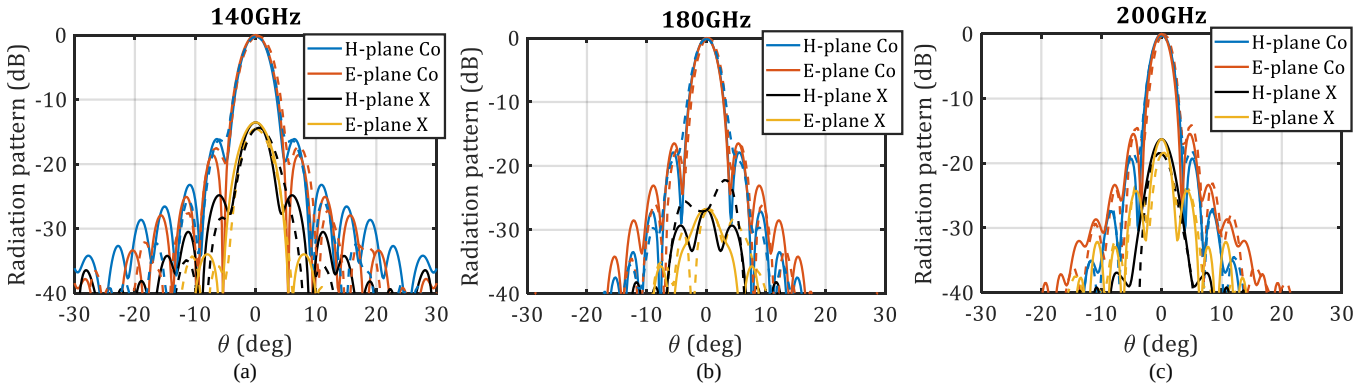

Fig. 8. Lens CP far-field patterns for the broadside beam. Solid line: FW simulations; dashed line: far-field from near-field measurements. E-, H- and D-planes are defined here with respect to the double-slot linear polarization.

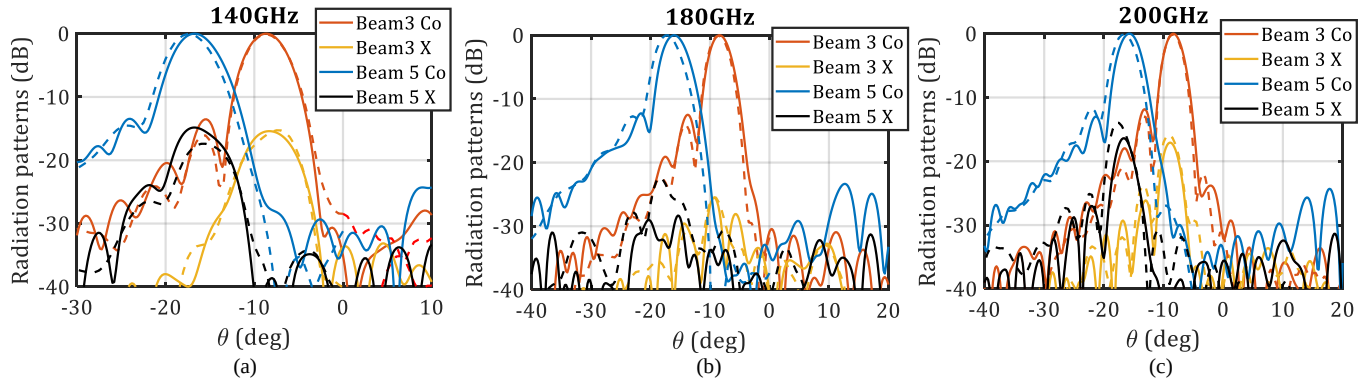

Fig. 9. Lens CP far-field patterns for the beams steering at 8.4deg (beam 3) and 16deg (beam5), normalized to their maximum co-polar amplitude. The steering is performed within the LP double-slot H-plane. The beams correspond to feed displacements, d = 0.09D and 0.19D. Solid line: FW simulations; dashed line: far-field from near-field measurements.

A similar approach was proposed in [32], where reflection measurements were performed in the antenna far-field using a metal plate and a corner reflector, extracting the CP antenna AR. Here instead we propose to place the metal reflector in the lens near-field region, at 1cm distance from the aperture, where the radiated fields are well-collimated with nearly planar phase front, thanks to the high aperture efficiency of the proposed lens antenna [1]. In that case, the field can be well predicted by performing a GO propagation. This assumption was validated in [1] by measuring the coupling between two LP lenses, and comparing with full wave simulations. The CP lens self-coupling for the first order rays can be calculated quasi-analytically using a GO approach combined with the analysis of the antenna in reception.

In order to perform the analysis in reception in this case, instead of an ideal plane-wave as previously explained, the incident field on the lens evaluated in reception is the field radiated by the same lens, reflected back at the metallic plate. The reaction integral to estimate V_{oc} is here calculated on the plane where the reflector is placed, S_r, as shown in Fig. 12a.

The field radiated by the lens in transmission mode, $\vec{E}_{GO}^{S_r,Tx}$, is calculated on S_r using a GO approach, as explained in [1], assuming that the rays are propagating out of the lens only in z-direction. Under this assumption, only field components tangent to the metallic plate are present in $\vec{E}_{GO}^{S_r,Tx}$, and therefore the reflected field, used as incident field in the analysis of the antenna in reception, can be approximated as $\vec{E}_{GO}^{S_r,Rx} = -\vec{E}_{GO}^{S_r,Tx}$. V_{oc} becomes in this case

$$V_{oc} \approx \frac{2}{\zeta_0}\int_0^{2\pi}\int_0^{D/2} \vec{E}_{GO}^{S_r,Tx}(\rho,\phi)\cdot\vec{E}_{GO}^{S_r,Rx}(\rho,\phi)\,\rho\,d\rho d\phi \quad (5)$$

being D the lens diameter. The coupling efficiency can be calculated as in (3), being in this case $P_{in} = P_{rad}$. Both reflected and transmitted fields can be formulated in terms of CP components, as proposed in [32]. In this way, the dot product $\vec{E}_{GO}^{S_r,Tx}\cdot\vec{E}_{GO}^{S_r,Rx} = 4E_{RH}E_{LH}$, being E_{RH} and E_{LH} the magnitudes of respectively the right and left handed polarized field components. Although the AR cannot be calculated from this single measurement [32], the AR and measured coupling minima are coincident when the AR equals 0dB.

The results of this analysis are shown in Fig. 12b, with a minimum reflection at 170GHz, where the calculated lens AR optimum appears (Fig. 7a). The estimated waveguide loss [1] and dielectric loss in the lens, obtained from FW simulations, have been added to the quasi-analytical calculation, in order to perform a fair comparison with the measured results. Time gating has been applied to the measured signal, in order to cancel the effect of multiple reflections and account only for the first reflected wave in the metal plate, as in the quasi-analytical evaluation. The time-gated measurement results are reported in Fig. 12b, showing a very good agreement with the quasi-analytical calculation.

B. Coupling CP-LP Lenses

The near-field coupling between a LP lens [1] and the fabricated CP lens has been measured with two purposes: derive the lens AR and validate the simulated lens η_{rad}, in order to estimate the lens maximum gain. This coupling can be as well calculated semi-analytically with an analysis of the antenna in reception.

The field radiated by the LP lens, $\vec{E}_{GO-LP}^{S_c}$, is calculated in the plane between both lenses, S_c in Fig. 13a, with a GO approach, and taken as incident field impinging on the CP lens. In the same way, the field transmitted by the CP lens, $\vec{E}_{GO-CP}^{S_c}$, is calculated at S_c, where the reaction integral is performed to calculate V_{oc} as

$$V_{oc} = \frac{2}{\zeta_0}\int_0^{2\pi}\int_0^{D/2} \vec{E}_{GO-LP}^{S_c}(\rho,\phi)\cdot\vec{E}_{GO-CP}^{S_c}(\rho,\phi)\,\rho\,d\rho d\phi \quad (6)$$

and the coupling efficiency can be calculated as in (3), being in this case P_{in} the power radiated by the LP lens feeder. V_{oc} is calculated with the LP lens in two polarization orientations, parallel and orthogonal to the CP lens feeder ($V_{oc}^{\parallel}$ and $V_{oc}^{\perp}$), as shown in Fig. 13a. Fig. 14a shows the magnitude of the calculated coupling efficiency for both LP orientations, $c_{\parallel}$ and $c_{\perp}$, where the estimated waveguide and dielectric loss have been as well added to perform a fair comparison with the measurement results. Fig. 14a shows as well the phase difference between $V_{oc}^{\parallel}$ and $V_{oc}^{\perp}$.

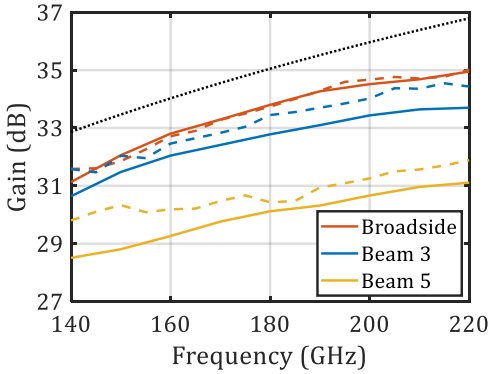

Fig. 10. Maximum gain for the lens CP co-polar components. Solid line: FW simulations; dashed line: measurements.

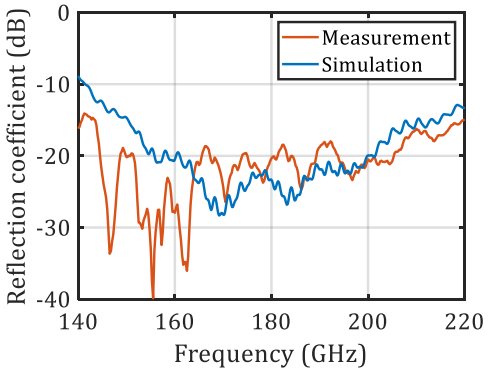

Fig. 11. Reflection coefficient for the CP lens.

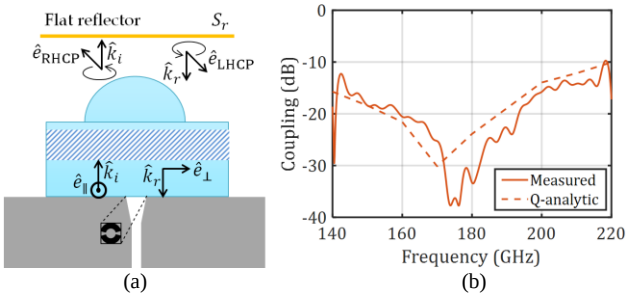

Fig. 12. a) Measurement setup for CP lens self-coupling. The fields and propagation constants are reported for the central ray. $\hat{e}_{\parallel}$ and $\hat{e}_{\perp}$ are defined as in Fig. 2b. b) CP lens self-coupling results. Quasi-analytic: reaction integral between PO fields. Measurements: reflection coefficient time gated to consider only first order reflected rays, and to eliminate reflections at WG taper and double-slot.

The CP lens AR at broadside can be calculated using $V_{oc}^{RH} = V_{oc}^{\parallel} - jV_{oc}^{\perp}$ and $V_{oc}^{LH} = V_{oc}^{\parallel} + jV_{oc}^{\perp}$ in equation (4). The field generated by the LP lens, impinging on the CP lens, is very close to the one of an ideal LP plane wave. Therefore, the AR derived from this measurement is almost overlapping with the AR calculated from the coupling to an ideal plane-wave (Section III.C), as shown in Fig. 14c. The small difference between both AR calculations is related to the different field amplitude taper and phase with respect to the ideal plane-wave case, taken as incident field in the analysis of the antenna in reception.

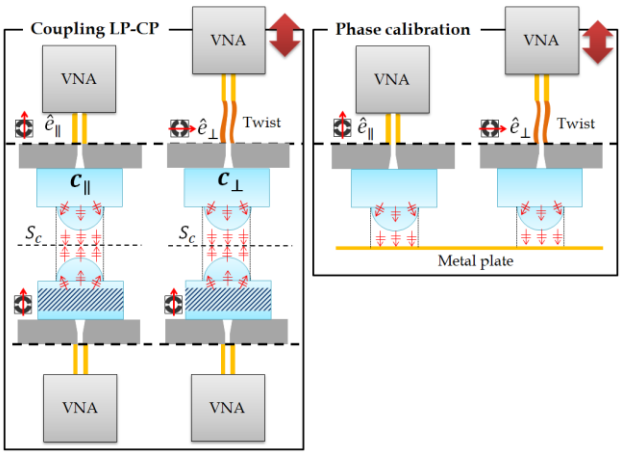

(a) (b)

Fig. 13. Measurement setup for a) coupling between LP lens (on top) and CP lens (bottom) and b) phase calibration between parallel and orthogonal coupling measurements. The top view of the LW feeder double-slot and e-field unit vector is shown for each lens. Calibration planes are marked with dashed lines.

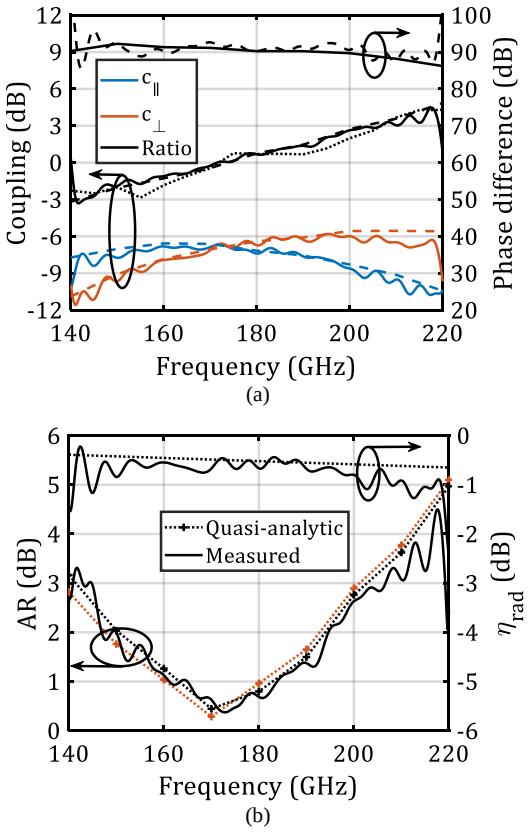

Fig. 14. a) Left axis: $c_\parallel$ and $c_\perp$ magnitude. Full line: measurements. Dashed line: quasi-analytic calculation. All include dielectric and waveguide loss. The ratio between $c_\parallel$ and $c_\perp$ is displayed as well. Dotted line: for comparison, radiated power ratio between parallel and orthogonal near-field measurements is also shown. Right axis: phase difference between $c_\parallel$ and $c_\perp$; solid line: time-gated measurements, dotted line: quasi-analytic model. b) Left axis: AR estimated from coupling to a LP lens field (black) and to a plane wave with uniform amplitude (red). Right axis: CP lens antenna radiation efficiency, excluding waveguide ohmic losses.

The coupling measurements have been performed placing the lenses at 2cm distance. From these measurements, complex coupling coefficients between both lenses, $c_\parallel$ and $c_\perp$, are evaluated. In order to rotate the LP lens polarization direction, a waveguide twist has been introduced between the Vector Network Analyzer (VNA) and the lens antenna. In this way, the VNA does not need to be rotated, which could degrade the VNA phase calibration. The twist has been characterized with one-port Short-Open-Load (SOL) measurements, and the results used to calibrate $c_\perp$.

Phase calibration: To obtain a good relative phase measurement between $c_\parallel$ and $c_\perp$, not only the twist S-parameters should be known, but also its exact length, so that both measurements are performed with the LP and CP lenses at the exact same distance. A fine correction of the twist estimated length was done by measuring the phase of the reflected wave from a metal plate, as shown in Fig. 13b. In order to consider only the first order waves reflected at the metal plate, time gating has been applied to both measurements. After correcting the twist estimated length in $+50\mu m$, the phase error decreases from 15 deg to 2deg in the whole frequency band. The reproducibility of this length correction has been verified by mounting the setup and performing the coupling measurements several times, and later on with near-field measurements.

Power coupling measurements: In the quasi-analytical model, only the first order transmitted rays are considered. Therefore, time gating has been applied to the measurements, performed with the setup reported in Fig. 13a, in order to cancel the effect of multiple reflections. Fig. 14a shows the time-gated measurement for $c_\parallel$ and $c_\perp$ and the phase difference between both, in good agreement with quasi-analytical results. The AR has been calculated from the coupling measurements using $V_{oc}^{\parallel} = c_\parallel$ and $V_{oc}^{\perp} = c_\perp$, showing good agreement with the quasi-analytic results (Fig. 14b). Being $c_\parallel$ and $c_\perp$ the couplings related to respectively orthogonal field components, the power coupled from both measurements can be used to validate the antenna η_{rad}. The estimated η_{rad} and the one obtained from the coupling measurements are shown in Fig. 14b, excluding waveguide loss. The maximum difference between both is 0.5dB, which includes measurement tolerances (coupling and twist characterization), tolerances in both LP and CP prototypes fabrication, and errors in the estimation of waveguide and dielectric losses.

C. Near-Field Measurements

In order to obtain the far-field patterns for the broadside and steered beams, the lens near-fields have been measured with a linear polarized open-ended waveguide probe. Several positioning holes in the split-block allow placing the lens with integrated polarizer in different lateral positions w.r.t. the feeder, in order to generate the broadside and steered beams, as shown in [1]. Two measurements have been performed for each beam, rotating the LP probe polarization to characterize both orthogonal components. The twist S-parameters and length have been considered and compensated likewise. The near-fields have been measured on a $50x50mm^2$ plane with $680\mu m$ distance between samples, 50mm above the lens

aperture. For the beams steering at 8.4deg and 16deg, the near-field measurement plane has been displaced laterally respectively 8mm and 17mm w.r.t. the lens center, in order to properly measure the field associated to the tilted rays.

The power ratio between both orthogonal LP near-field measurements for the broadside beam is coincident with the one estimated from the coupling measurements, as shown in Fig. 14a, confirming the consistency between both results. The normalized CP far-field patterns obtained from each pair of LP near-field measurements are shown in Fig. 8 and Fig. 9, with good agreement with the FW simulation results. Fig. 10 displays the measured maximum gain for the broadside and steered beams, including dielectric loss in the polarizer and lens. The gain has been estimated with the maximum directivity from the far-field measurements and the FW η_{rad} (Fig. 14b), validated with the coupling measurements. The gain for the steered beams has been normalized to the measured power radiated by the broadside beam, in order to account for the power scattered outside of the measurement plane. The differences between FW simulated and measured results are related to the measurement tolerances in the two near-field measurements, their relative position and phase, and fabrication tolerances. Fig. 7 shows the measured η_{ap} for the broadside beam, higher than 75% in the whole frequency band. In Fig. 7, the AR obtained from the measured CP far-field at broadside and steered beams is displayed, reaching a 3dB AR relative bandwidth of 35%. The measured far-field AR includes the effect of multiple reflections, as no time-gating has been applied. All results present good agreement with FW simulation results, validating the prototype performance, as well the phase calibration method applied (Fig. 13b). Table I presents a summary of the performance reached in our design, compared to the most relevant designs of CP antennas found in the literature.

TABLE I
MEASURED PERFORMANCES OF CP ANTENNAS*

Ref.	f_0 (GHz)	Gain f_0 (dB)	–3dB AR BW (%)	Min. η_{ap} (%)	Max. L_σ (dB)	Max. SLL (dB)
[12]	29	20.8	>14.6	17	2.3	–15
[15]	58.5	21.4	29	87.5	3	–12
[16]	34/500	11.2	>35	-	-	–15
[17]	115	18	37	-	-	–10
[18]	140	31.7	>28	*55*	1.9	–13
[24]	30	23.4	2.6	65	2	–10
This work	180	34	35	75	0.6	–15

(*) References in bolt present multi-beam capability. Values in italic have been extracted from the articles.
(**) L_σ comprises ohmic and dielectric loss.

V. CONCLUSION

In this work, a G-band lens with an integrated dielectric grid polarizer has been presented, achieving full-wave simulated aperture efficiency higher than 75% and axial ratio lower than 3dB over 35% relative bandwidth. The CP lens reaches more than 30 dB of gain with only 0.65 dB dielectric loss. The proposed new polarizer unit cell presents excellent transmission properties over the whole bandwidth, and can be easily fabricated for these high frequency bands through standard milling techniques.

A semi-analytical model has been used to analyze the full system feeder-polarizer-lens, based on SGF and an analysis in reception of the lens. This approach allows us to make a very time-efficient optimization of the feeder-polarizer-lens system and presents very good agreement with the measurements. Thanks to this analysis, state-of-the-art performances have been reached with this CP lens antenna.

APPENDIX: TRANSMISSION LINE MODEL

In order to calculate the circularly-polarized feeder radiation patterns inside the lens, the transmission line model in Fig. 3 has been applied. The LW air cavity and lens dielectric medium in which the polarizer is inserted are modelled as isotropic media, with different transmission lines for the TE and TM mode propagation. The polarizer is treated as a homogeneous anisotropic slab inserted in the isotropic lens medium, with a certain height ($z_{top} - z_{bot}$). The polarizer S-parameters correspond to a 4x4 matrix coupling the TM and TE modes for each θ_i and ϕ_i incident angle. The S-parameters are calculated with FW Floquet-mode based simulations for a single unit cell, for the different θ_i, ϕ_i. Finally, the lens is modelled as a semi-infinite dielectric medium, neglecting the effect of multiple reflections in the lens-air interface.

The discontinuity in the tangent electric field at the source (double-slot in the ground plane) is represented by two equivalent tangent magnetic sources, V_g^{TM} and V_g^{TE}

$$V_g^{TE} = -\frac{\vec{M}_s \cdot \hat{k}_\rho}{jk_\rho} \tag{7a}$$

$$V_g^{TM} = -\frac{\vec{M}_s \cdot \hat{\alpha}}{jk_\rho} \tag{7b}$$

being $\vec{M}_s$ the Fourier transform of the double-slot equivalent magnetic currents, $k_\rho = \sqrt{k_x^2 + k_y^2}$, $\hat{k}_\rho = \frac{1}{k_\rho}\left(k_x\hat{x} + k_y\hat{y}\right)$ and $\hat{\alpha} = \frac{1}{k_\rho}\left(k_x\hat{y} - k_y\hat{x}\right)$. The analytical expression for the double-slot currents is given and validated in [1]. After finding the solutions for the voltages and currents at every z-quote, the spectral fields can be calculated as

$$\vec{\bar{E}}_{TM}\left(\vec{k}_\rho, z\right) = -\frac{j\zeta k_\rho^2}{k} I_{TM}\left(\vec{k}_\rho, z\right)\hat{z} + jk_\rho V_{TM}\left(\vec{k}_\rho, z\right)\hat{k}_\rho \tag{8a}$$

$$\vec{\bar{E}}_{TE}\left(\vec{k}_\rho, z\right) = -jk_\rho V_{TE}\left(\vec{k}_\rho, z\right)\hat{\alpha} \tag{8b}$$

where ζ is the medium characteristic impedance. The far-field of the LWA feeder illuminating the semi-infinite dielectric medium through the polarizer can be calculated using the asymptotic expression as

$$\vec{E}_a^{GP}(\vec{r}) \approx 2jk_{zs}\vec{\bar{E}}\left(\vec{k}_{\rho s}, z\right)e^{jk_{zs}z}\frac{e^{-jk_d r}}{4\pi r} \tag{9}$$

where $\vec{\bar{E}} = \vec{\bar{E}}_{TM} + \vec{\bar{E}}_{TE}$, $k_d = k_0\sqrt{\varepsilon_r}$, $k_{\rho s} = k_d \sin\theta$ and $k_{zs} = k_d \cos\theta$. The origin of the coordinate system is here placed on the ground plane.

REFERENCES

[1] M. Arias Campo, D. Blanco, S. Bruni, A. Neto, and N. Llombart "On the use of Fly's eye lenses with leaky wave feeds for wideband wireless communications," *IEEE Trans. Antennas Propag.*, accepted for publication.

[2] N. Llombart, D. Emer, M. Arias Campo, and E. McCune "Fly's eye spherical antenna system for future Tbps wireless communications," *in Proc. European Conf. on Antennas and Propag. (EuCAP)*, Paris, France, Apr. 2017.

[3] N. Yoneda, M. Miyazaki, H. Matsumura, and M. Yamato "A design of novel grooved circular waveguide polarizers," *IEEE Trans. Microw. Theory and Techn.*, vol. 48, no. 12, , pp. 2446–2452, Dec. 2000.

[4] S. Wang, C. Chien, C. Wang, and R. Wu "A circular polarizer designed with a dielectric septum loading," *IEEE Trans. Microw. Theory and Techn.*, vol. 52, no. 7, pp. 1719–1723, July 2004.

[5] M. Letizia, B. Fuchs, A. Skrivervik, and J.R. Mosig, "Circularly polarized homogeneous lens antenna system providing multibeam radiation pattern for HAPS," *Radio Science Bulletin*, no. 332, pp. 18–28, Mar. 2010.

[6] Y. Cai, Y. Zhang, Z. Qian, W. Cao, and S. Shi "Compact wideband dual circularly polarized substrate integrated waveguide horn antenna," *IEEE Trans. Antennas Propag.*, vol. 64, no. 7, pp. 3184–3189, July 2016.

[7] X. Cheng, Y. Yao, T. Yu, Z. Chen, J. Yu, and X. Chen "Analysis and design of a low-cost circularly polarized horn antenna," *IEEE Trans. Antennas Propag.*, *IEEE Trans. Antennas Propag.*, vol. 66, no. 12, pp. 7363–7367, Dec. 2018.

[8] J. Wu, Y. J. Cheng, H. B. Wang, Y. C. Zhong, D. Ma, and Y. Fan, "A wideband dual circularly polarized full-corporate waveguide array antenna fed by triple-resonant cavities," *IEEE Trans. Antennas Propag.*, vol. 65, no. 4, pp. 2135–2139, Apr. 2017.

[9] M.-A. Joyal and J.-J. Laurin, "Analysis and design of thin circular polarizers based on meander lines," *IEEE Trans. Antennas Propag*., vol. 60, no. 6, pp. 3007–3011, June 2012.

[10] S. M. A. M. H. Abadi and N. Behdad, "Wideband linear-to-circular polarization converters based on miniaturized-element frequency selective surfaces," *IEEE Trans. Antennas Propag.*, vol. 64, no. 2, pp. 525–534, Feb. 2016.

[11] D. Blanco and R. Sauleau "Broadband and broad-angle multilayer polarizer based on hybrid optimization algorithm for low-cost Ka-band applications," *IEEE Trans. Antennas Propag.*, vol. 66, no. 4, pp. 1874–1881, Apr. 2018.

[12] L. Di Palma, A. Clemente, L. Dussopt, R. Sauleau, P. Potier, and P. Pouliguen, "Circularly-polarized reconfigurable transmitarray in Ka-band with beam scanning and polarization switching capabilities," *IEEE Trans. Antennas Propag.*, vol. 65, no. 2, pp. 529–540, Feb. 2017.

[13] S. Mener, R. Gillard, R. Sauleau, A. Bellion, and P. Potier, "Dual circularly polarized reflectarray with independent control of polarizations," *IEEE Trans. Antennas Propag.*, vol. 63, no. 4, pp. 1877–1881, Apr. 2015.

[14] J. Wang, Z. Shen, W. Wu, and K. Feng "Wideband circular polarizer based on dielectric gratings with periodic parallel strips," *Optics Express*, vol. 23, no. 10, pp. 12533–12543, May 2015.

[15] K.X. Wang and H. Wong, "Design of a wideband circularly polarized millimeter wave antenna with an extended hemispherical lens," *IEEE Trans. Antennas Propag.*, vol. 66, no. 8, pp. 4303–4308, Aug. 2018.

[16] Y. Liu, H. Lu, Y. Wu, M. Cui, B. Li, P. Zhao, and X. Lv "Millimeterwave and teraherz waveguide-fed circularly polarized antipodal curvedly tapered slot antennas," *IEEE Trans. Antennas Propag.*, vol. 64, no. 5, pp. 1607–1614, May 2016.

[17] S. Bhardwaj and J. L. Volakis, "Hexagonal waveguide based circularly polarized horn antennas for sub-mm-wave/terahertz band," *IEEE Trans. Antennas Propag.*, vol. 66, no. 7, pp. 3366–3374, July 2018.

[18] M. M. Zhou and Y. J. Cheng, "D-Band high-gain circular-polarized plate array antenna," *IEEE Trans. Antennas Propag.*, vol. 66, no. 3, pp. 1280–1287, Mar. 2018.

[19] M. Euler, V. Fusco, R. Dickie, R. Cahill, and J. Verheggen, "Sub-mm wet etched linear to circular polarization FSS based polarization converters," *IEEE Trans. Antennas Propag.*, vol. 59, no. 8, pp. 3103–3106, Aug. 2011.

[20] M. Mutlu, A. E. Akosman, and E.Ozbay, "Broadband circular polarizer based on high-contrast gratings," *Optics Letters*, vol. 37, no. 11, pp. 2094–2096, June 2012.

[21] T. Kämpfe, P. Sixt, D. Renaud, A. Lagrange, F. Perrin, and O. Parriaux, "Segmented subwavelength silicon gratings manufactured by high productivity microelectronic technologies for linear to radial/azimuthal prolarization conversion," *Optical Engineering*, vol. 53, no. 10, pp. 107105-1–107105-5, Oct. 2014.

[22] K.B.Cooper, N. Llombart, G. Chattopadhyay, B. Dengler, R. E. Cofield, C. Lee, S. Filchenkov, and E. Koposova, "A grating-based circular polarization duplexer for submillimeter-wave transceivers," *IEEE Microw. Wireless Compon. Lett.*, vol. 22, no. 3, pp. 108–110, Mar. 2012.

[23] E. Doumanis, G. Goussetis, R. Dickie, R. Cahill, P. Baine, M. Bain, V. Fusco, J. A. Encinar, and G. Toso, "Electronically reconfigurable liquid crystal based mm-wave polarization converter," *IEEE Trans. Antennas Propag.*, vol. 62, no. 4, pp. 2302–2307, Apr. 2014.

[24] X. Wu, G. V. Eleftheriades and T. E. van Deventer-Perkins "Design and characterization of single- and multiple-beam mm-wave circularly polarized substrate lens antennas for wireless communications," *IEEE Trans. Microw. Theory and Techn.*, vol. 49, no. 3, pp. 431–441, Mar. 2001.

[25] M. Arias Campo, G. Carluccio, D. Blanco, S. Bruni, O. Litschke, and N. Llombart, "Dielectric-grating in-lens polarizer for beyond 5G communications," *in Proc. 44th Int. Conf. on Infrared, Millim. and THz Waves (IRMMW-THz)*, Paris, France, Sept. 2019.

[26] N. Llombart, G. Chattopadhyay, A. Skalare, and I. Mehdi, "Novel terahertz antenna based on a silicon lens fed by a leaky wave enhanced waveguide", *IEEE Trans. Antennas Propag*., vol. 59, no. 6, pp. 2160–2168, Jun. 2011.

[27] A. Neto, O. Yurduseven, N. Llombart, and A. Freni; "Antennas in reception," *in Proc. European Conf. on Antennas and Propag. (EuCAP)*, Lisbon, Portugal, Apr. 2015.

[28] N. Llombart, B. Blazquez, A. Freni, and A. Neto, "Fourier Optics for the analysis of distributed absorbers under THz focusing systems," *IEEE Trans. THz Sci. and Technol.*, vol. 5, no. 4, pp. 573–583, July 2015.

[29] C. A. Balanis, *Advanced Engineering Electromagnetics*, 1st Edition, 154–179, John Wiley and Sons, New York, USA, 1989.

[30] CST Studio Suite, Available "https://www.3ds.com/products-services/simulia/products/cst-studio-suite".

[31] EMPIRE XPU, Available "http://www.empire.de".

[32] S. Bhardwaj, N. K. Nahar, and J. L. Volakis, "Novel phaseless gain characterization for circularly polarized antennas at mm-wave and THz frequencies," *IEEE Trans. Antennas Propag*., vol. 63, no. 10, pp. 4263–4270, Oct. 2015.

[33] B. Y. Toh, R. Cahill, and V. Fusco, "Understanding and measuring circular polarization," IEEE Trans. Educ., vol. 46, no. 3, pp. 313–318, Aug. 2003.